Check for updates

Tuning the structural, electronic and dynamical properties of Janus $M_4X_3Y_3$ (M = Pd, Ni and Co; X,Y = S, Se and Te) monolayers: a DFT study†

Ismail Eren[a] and Berna Akgenc [ID] *[b]

Based on density functional theory, the structural, electronic and vibrational properties of two-dimensional transition metal chalcogenides M_2X_3 and their Janus type $M_4X_3Y_3$, where M = Pd, Co and Ni and X = Se, S and Te, are investigated. Motivated by the successful synthesis of a 2D Pd_2Se_3 monolayer and the proof of the dynamical stability of Ni_2Se_3 and Co_2Se_3 monolayers, in terms of the phonon band dispersions, we have systemically studied the fundamental physical properties of Janus transition metal chalcogenides, such as their structural, phonon and thermodynamic stability and their electronic and mechanical properties. Our results show that Janus structures of $M_4X_3Y_3$ are energetically favorable and dynamically stable. The *ab initio* molecular dynamic simulations (AIMD) results clearly prove that they kept their thermal stability at room temperature. We have demonstrated their structural, electronic and vibrational properties and Raman spectra. The electronic band dispersions show that monolayer Co_2Se_3 shows half-metal properties with a moderate band gap (1.01 eV), Pd_2Se_3 has a 1.42 eV direct band gap, while Ni_2Se_3 has a 1.38 eV indirect band gap. $Pd_4Se_3S_3$, $Pd_4Se_3Te_3$ and $Pd_4S_3Te_3$ are indirect band gap semiconductors with band gaps of 1.22 eV, 1.05 eV and 0.61 eV, respectively. $Ni_4Se_3S_3$, $Ni_4Se_3Te_3$ and $Ni_4S_3Te_3$ are indirect band gap semiconductors with band gaps of 1.61 eV, 0.77 eV and 0.49 eV, respectively. While pristine Co_2Se_3 is shown to have half-metallicity (HM), the HM behaviour of the Janus $Co_4Se_3Te_3$ and $Co_4S_3Te_3$ monolayers disappear and $Co_4Se_3S_3$ remains a HM with a moderate band gap of 0.85 eV. In addition, the Raman spectra of these Janus materials are shown to exhibit totally distinctive features as compared to those of the pristine materials. This work reveals the important material properties of Janus type $M_4X_3Y_3$ monolayers, where M = Pd, Co and Ni and X = Se, S and Te, which could have wide applications in new functional devices.

1 Introduction

Since the successful synthesis of graphene, two-dimensional (2D) materials have received increasing interest in their unique properties.[1] Due to the band gap of graphene being zero limiting its electronic applications, there has been emerging interest in other 2D materials beyond graphene,[2–4] such as hexagonal boron nitride (h-BN),[5–7] MXenes[8–14] and transition metal di-chalco-genides (TMDCs).[15–18] The general formula for TMDCs is MX_2; where M is the transition metal and X is the double chalcogenide (S, Se or Te), and they are mostly in the honeycomb lattice of the 2H phase, such as MoS_2, $MoSe_2$ and WS_2.[19,20]

Monolayer $PdSe_2$, which is a special 2D TMDC material, possesses an uncommon pentagonal structural motif and

anisotropic properties[21] and has been successfully synthesized *via* mechanical exfoliation.[22] While bulk $PdSe_2$ has a narrow band gap of 0.03 eV, monolayer $PdSe_2$ has an indirect band gap of about 1.43 eV due to the occurrence of a remarkable quantum confinement effect. The discovery of pentagonal $PdSe_2$ makes the emerging physics related to the low symmetry structure possible and it has significant potential in piezoelectric,[23,24] optoelectronic[25–27] and thermoelectronic[28–32] applications. An alternative phase of 2D TMDCs is formed as a descendent of the bulk phase which is indicated in the chemical composition: M_2X_3 (M = Pd, Ni and Co; X= S, Se and Te). Pd_2Se_3, which is the one of the members of the M_2X_3 family, was synthesized by cleaving it from $PdSe_2$[33] by Li *et al.* They demonstrated that Se vacancies in the pristine $PdSe_2$ reduce the distance between the layers, melding the two layers into one, thus, it creates a new form of the Pd_2Se_3 monolayer. Pd_2Se_3 is unique in several aspects: first, the thermodynamically and kinetically stable Pd_2Se_3 is a semiconducting material with a moderate band gap of 0.45 eV and its carrier mobility (178.02 cm^2 V^{-1} s^{-1}) is

[a] Department of Physics, Izmir Institute of Technology, Izmir, 35430, Turkey
[b] Department of Physics, Kirklareli University, Kirklareli, 39100, Turkey.
  E-mail: berna.akgenc@klu.edu.tr; Tel: +90 0530 090 5208
† Electronic supplementary information (ESI) available. See DOI: 10.1039/d1cp01916c

comparable to that of the MoS_2 monolayer.[34,35] Second, monolayer Pd_2Se_3 is calculated to be a highly efficient thermoelectric material, owing to extremely low lattice thermal conductivity in conjunction with a high power factor, which could not be fulfilled by traditional TMD monolayers.[36] Third, its strong interlayer interactions, moderate band gap, novel anisotropic properties, good current–voltage characteristics and excellent absorption in a wide range of the solar spectrum render it desirable for photovoltaic applications.[37] In addition, the thermal and optical properties, defects and grain boundaries of 2D Pd_2Se_3 have deeply investigated by Chen *et al.*[38] They identified the cross-shaped point defects rebuilt from Se_B vacancies (V-Se_B), as well as adatoms. These vacancies exhibit self-healing behaviour *via* migrating to the edge instead of forming line vacancies like other TMCs, suggesting the high mobility of the V-Se_B under an electron beam. The distinct monolayer Pd_2Se_3 defects can enrich the structural knowledge of 2D materials and offer more possibilities for exploiting the versatile properties of 2D materials through defect engineering. Moreover, Lv *et al.* have extended the study to M_2Se_3 monolayers, where M = Pd, Co or Ni, to understand their structural stabilities and electronic, magnetic and mechanical properties. They have demonstrated that M_2Se_3 monolayers have an intrinsic large out-of plane negative Poisson's ratio (NPR) and superior mechanical flexibility, with their resistance of critical strain (50–60%) being two times greater than those of well-known 2D materials. Co_2Se_3 was found to be half-metallic and ferromagnetic with a high Curie temperature (>700 K).[39] Furthermore, Xiong *et al.* have studied the mechanical, electronic and optical properties of orthorhombic M_2X_3 (M = Ni and Pd; X = S, Se and Te) (especially Ni_2Se_3 and Pd_2S_3) and their potential applications in photocatalytic water splitting within the visible and ultraviolet light regions.[40]

An alternative way to make new 2D materials is modified 2D Janus materials, which introduces out-of-plane structural symmetry. The formation of 2D Janus materials that possess different atoms on two faces has been achieved for the tailoring of 2D materials designed at the atomic level. Although Janus 2D materials do not exist in nature, Janus monolayers of TMDs, with the MoS_2 structure modified as S–Mo–Se sandwiched layers, has also been successfully synthesized[41,42] for the first time. The characterization results showed that Janus 2D materials may have unique properties, such as strong Rashba spin splitting, a second-harmonic generation (SHG) response, large piezoelectric effect and good catalytic performance. These new materials have potential engineering applications in such fields as sensors, actuators and novel electromechanical devices.[43–45] According to our knowledge, Janus structures of M_2X_3 (M = Ni, Pd and Co; X = S, Se and Te) monolayers have not been reported up to this date. Our study could motivate experimental efforts in achieving Janus structures of M_2X_3 monolayers for new applications in electronic, optoelectronic and thermoelectric devices.

Inspired by M_2X_3's unique properties, we have constructed possible Janus structures of M_2X_3, which are classified into three forms: palladium derivatives ($Pd_4Se_3S_3$, $Pd_4Se_3Te_3$ and $Pd_4S_3Te_3$), cobalt derivatives ($Co_4Se_3S_3$, $Co_4Se_3Te_3$ and $Co_4S_3Te_3$) and nickel derivatives ($Ni_4Se_3S_3$, $Ni_4Se_3Te_3$, $Ni_4S_3Te_3$), to investigate their

structural, electronic, vibrational and high temperature dynamical stability properties using first principles methods. The paper is organized as follows: details of the computational methodology are given in Section 2. The ground-state structures of the pristine and Janus structures of M_2X_3 (M = Ni, Pd and Co; X = S, Se and Te) monolayers are obtained and their dynamical stabilities are tested by phonon spectrum analysis, Raman spectra and *ab initio* molecular dynamic calculations. In addition, the electronic properties of the pristine and Janus structures of M_2X_3 are also given in Section 3. Finally, the results are concluded in Section 4.

2 Computational methodology

For the first principles calculations, the plane-wave basis projector augmented wave (PAW) method was employed in the framework of density functional theory (DFT).[46] The generalized gradient approximation (GGA) in the Perdew–Burke–Ernzerhof (PBE)[47] form was used for the exchange–correlation potential, as implemented in the Vienna *ab initio* simulation package (VASP).[48,49] The van der Waals (vdW) correction to the GGA functional was included using the Becke–Johnson (BJ) damping of the DFT-D3 method.[50] To consider the more precise band structures, electronic calculations of Pd_2Se_3, Ni_2Se_3 and Janus M_2X_3 (M = Pd and Ni; X = S, Se and Te) were also performed using the spin–orbit coupling (SOC) effects and hybrid functional (HSE06) approach.[51] In addition, to consider the strong correlation effects between the d-orbitals of Co atoms, electronic structure calculations of Co_2Se_3 and Co-based Janus M_2X_3 (M = Co; X = S, Se and Te) monolayers were performed using Dudarev's GGA+U approach.[52] In our calculations, the Hubbard on-site Coulomb parameter (U) was taken into consideration and the U value of the Co atom was set to be 3 eV. Analysis of the charge transfer in the structures was determined by the Bader technique.[53] Electronic and geometric relaxations of the pristine single-layer M_2Se_3 (M = Pd, Ni and Co) and Janus structures of the M_2X_3 (M = Ni, Pd and Co; X = S, Se and Te) monolayers were performed on 5- and 10-atom unit cells, respectively. The kinetic energy cut-off for plane-wave expansion was set to be at least 290 eV and the energy was minimized until its variation in the following steps became 10^{-5} eV. The Gaussian smearing method was employed for the total energy calculations and the width of the smearing was chosen to be 0.05 eV. The total Hellmann–Feynman forces in the unit were reduced to 10^{-4} eV Å^{-1} for the structural optimization. A minimum of $6 \times 6 \times 1$ Γ centered k-point samplings were used for the two primitive unit cells. To avoid interaction between the neighboring layers, a vacuum space of at least 25 Å was implemented in the calculations. To check the dynamic stability, we used the density functional perturbation theory (DFPT) using the small displacement methodology.[54,55] The force constant matrix was constructed by the slight displacements of a maximum $4 \times 4 \times 1$ supercell whose Brillouin zone (BZ) was sampled with a maximum of $6 \times 6 \times 1$ k-points by implementing the PHONOPY code,[56] depending on the unit cell size. We also increased the electronic degrees of freedom to 10^{-8} eV to ensure a reasonable convergence. The phonon frequencies and the corresponding

21140 | *Phys. Chem. Chem. Phys.*, 2021, **23**, 21139–21147

This journal is © the Owner Societies 2021

off-resonant Raman activities were calculated at the point of the BZ using the same methodology. Additionally, *ab initio* molecular dynamics simulations (AIMD) were performed to assess the thermal stability of the Janus structures of M_2X_3 (M = Ni, Pd and Co; X = S, Se and Te) monolayers. The initial configurations of these monolayers were annealed at room temperature (300 K). AIMD simulations in the *NVT* ensemble lasted for 10 ps with a time step of 1.0 fs and the temperature was controlled using the Nose–Hoover thermostat.

3 Results and discussion

3.1 Pristine M_2Se_3 (M = Pd, Ni and Co) monolayers

First, we have examined the geometric optimization of monolayer Pd_2Se_3, Co_2Se_3 and Ni_2Se_3, which show significant structural similarity. All of the geometric structures are built up with 10 atoms in a unit cell; 4 of the atoms are M type atoms (Pd, Co and Ni), which are sandwiched between 6 Se atoms which are placed half-and-half above and below the M type atoms (see Fig. 1). We have continued our calculations with Pd_2Se_3 and Ni_2Se_3, which have nonmagnetic (NM) ground states, while Co_2Se_3 has a ferromagnetic (FM) ground state, according to a previous theoretical study[39]. Due to the itinerant Co d-electrons, we have also considered antiferromagnetic (AFM) orderings (*i.e.*, AFM-Néel, AFM-Stripy, AFM-Zigzag, which are shown in Fig. S1 in the ESI†). The comparison of the minimum energies, which are obtained following the structural optimizations, including lattice constants, for each magnetic state, implies that the lowest energy configuration is FM for the Co-based Janus structure. This is due to the Co atom possessing the electronic configuration of $3d^7 4s^2$ and Co^{2+} has unpaired

electrons, which gives rise to the magnetic state of the Co-based Janus structure.

In our theoretical framework, the relaxed structural parameters, *i.e.*, the lattice parameters (*a* and *b*), of the two-dimensional Pd_2Se_3, Co_2Se_3 and Ni_2Se_3 structures are found to be 5.89 Å and 6.00 Å, 5.46 Å and 5.74 Å, and 5.37 Å and 5.82 Å, respectively. As shown in Table 1, the bond lengths (*d*) between the M atoms and the Se atoms vary between 2.45–2.53 Å, 2.32–2.38 Å and 2.31–2.37 Å (for M = Pd, Co and Ni, respectively). The vertical height (*h*), defined as the out of plane distance between the top and bottom X sublayers, is 3.86 Å for Pd_2Se_3, 3.74 Å for Co_2Se_3 and 3.75 Å for Ni_2Se_3. By comparing the pristine X_2Se_3 unit cells, the bond lengths and heights of Pd_2Se_3 are bigger than those of Co_2Se_3 and Ni_2Se_3. According to the Bader charge analysis, the Pd atom donates 0.15*e*, the Co atom donates 0.37*e* and the Ni atom donates 0.30*e* to the Se atoms. The cohesive energies (per atom) of the pristine X_2Se_3 (X = Ni, Pd, Co) structures were calculated using the following relation:

$$E_{Coh} = [E(X_2Se_3) - 4 \times E(X) - 6 \times E(Se)]/10 \qquad (1)$$

where $E_T(X_2Se_3)$ is the total energy of the X_2Se_3 (X = Ni, Pd and Co) monolayers and $E(X)$ and $E(Se)$ are the single isolated atom energies of Ni, Pd and Co and Se, respectively. The calculated cohesive energies E_{Coh} for Pd_2Se_3, Ni_2Se_3 and Co_2Se_3 are 3.73, 4.06 and 4.12 eV per atom, respectively. Our results indicate that they are energetically stable and these materials can be synthesized.

The vibrational properties, shown in Fig. 1(d–f), show that the 2D Pd_2Se_3, Co_2Se_3 and Ni_2Se_3 are dynamically stable, as previously demonstrated by Lv *et al.*[39] All of the structures have 30 phonon modes. The phonon modes with the highest frequencies at the Γ point are 252.7 cm^{-1}, 303.1 cm^{-1} and 315.1 cm^{-1} for Pd_2Se_3, Co_2Se_3 and Ni_2Se_3, respectively. The significant difference of the phononic calculation compared with earlier work[39] is the increase in the frequency of the S point of Co_2Se_3, with most of the phonon modes still having positive frequencies.

The band structures of the 2D Pd_2Se_3 and Ni_2Se_3 monolayers with the HSE + SOC calculation and Co_2Se_3 with the GGA+U calculation (the majority spin is colored in blue and the minority spin is in orange) were calculated and are presented in Fig. 2. Interestingly, it can be clearly seen that the FM Co_2Se_3 shows the half-metal property with a moderate band gap (1.01 eV) for the spin-up state (blue lines) while the band can cross the Fermi level for the spin-down state (orange lines). The NM Pd_2Se_3 and Ni_2Se_3 monolayers both show indirect band gaps. The Pd_2Se_3 monolayer has an 1.42 eV direct band
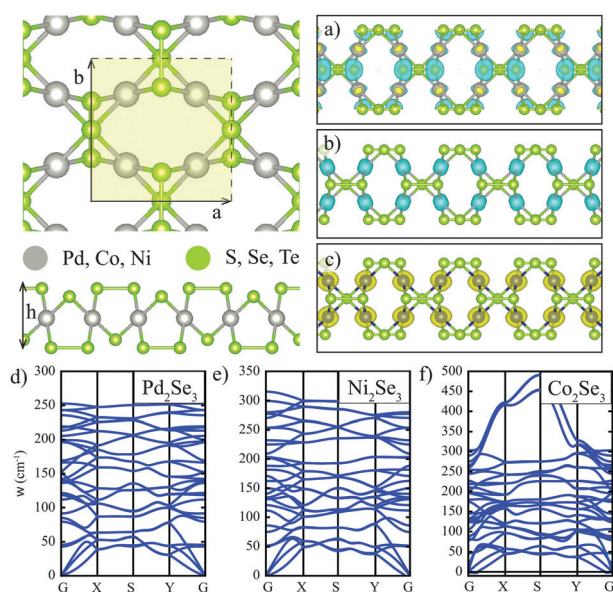

Fig. 1 The top and side views of the Janus monolayers of M_2Se_3 (M = Pd, Ni and Co) (top right); the corresponding charge distribution on the individual atoms (a) Pd_2Se_3, (b) Ni_2Se_3 and (c) Co_2Se_3. The phonon band dispersions for (d) Pd_2Se_3, (e) Ni_2Se_3 and (f) Co_2Se_3. The primitive unit cell is indicated by the red parallelogram representing the lattice vectors *a* and *b*.

Table 1 Calculated parameters for the pristine X_2Se_3 unit cell: lattice constants: *a* and *b*, M−Se bond lengths: *d*, vertical height: *h*, average charge transfer from the M type atom: ρ, cohesive energy per atom: E_{Coh} and electronic band gap: E_g

|	*a* (Å)	*b* (Å)	*d* (Å)	*h* (Å)	ρ (e)	E_{Coh} (eV)	E_g (eV)
Pd_2Se_3	5.80	6.00	2.45–2.53	3.86	−0.15	3.73	1.42
Ni_2Se_3	5.37	5.82	2.31–2.37	3.75	−0.30	4.06	1.38
Co_2Se_3	5.46	5.74	2.32–2.38	3.74	−0.37	4.12	—
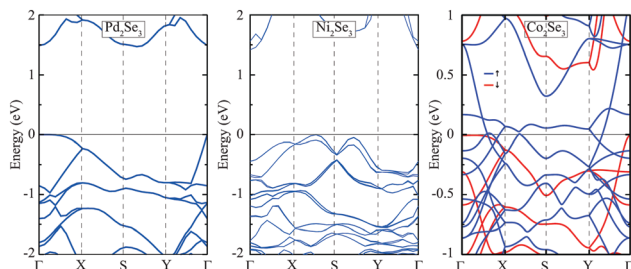
Fig. 2 Electronic band structures of Pd_2Se_3 and Ni_2Se_3 with the HSE + SOC calculation and Co_2Se_3 with the GGA+U calculation (the majority spin is colored in blue and the minority spin is in orange). The Fermi level is set to zero.

3.2 Janus $M_4X_3Y_3$ (M = Pd, Ni and Co; X,Y = S, Se and Te) monolayers

In this section, the Janus derivatives of the monolayers Pd_2Se_3, Co_2Se_3 and Ni_2Se_3 are investigated. While the sandwiched M type atom is Pd, Ni and Co atoms, the atoms at the two faces vary between Se, S and Te, thus, obtaining the form $M_4X_3Y_3$. In the following section, $Pd_4Se_3S_3$, $Pd_4Se_3Te_3$, $Pd_4S_3Te_3$, $Ni_4Se_3S_3$, $Ni_4Se_3Te_3$, $Ni_4S_3Te_3$, $Co_4Se_3S_3$, $Co_4Se_3Te_3$ and $Co_4S_3Te_3$ were investigated (Fig. 3).

3.3 Structural and electronic properties

In the geometric optimization calculations, the structural phases of $M_4X_3Y_3$ negligibly change with respect to their pristine structures. In the Pd derivatives, the lattice constant varies by a maximum of 0.24 Å. The Pd–Se distance shows a minor change in the Janus structures. In the Janus structures, the atomic composition of one face slightly alters the bond length of the other side. In the $Pd_4S_3Te_3$ material, the Pd–S and Pd–Te bond

Fig. 3 Side view (perspective) of the optimized geometric structures of the Janus $M_4X_3Y_3$ (M = Pd, Ni and Co; X,Y = S, Se and Te) monolayers with structural parameters (a, b, d and h).

Table 2 Calculated parameters for the Janus type $M_4X_3Y_3$, where M = Pd, Co and Ni and X = Se, S and Te: lattice constants: a b; M–X and M–Y distances are d_1 and d_2, respectively, vertical height: h, average charge transfer from the M type atom: ρ, cohesive energy per atom: E_{Coh} and electronic band gap: E_g

	a (Å)	b (Å)	d_1 (Å)	d_2 (Å)	ρ (e)	E_{coh} (eV)	E_g (eV)
$Pd_4Se_3S_3$	5.79	5.90	2.45–2.52	2.33–2.42	−0.20	3.85	1.22
$Pd_4Se_3Te_3$	5.94	6.24	2.46–2.54	2.61–2.67	+0.01	3.65	1.05
$Pd_4S_3Te_3$	5.85	6.06	2.35–2.43	2.63–2.67	−0.09	3.76	0.61
$Ni_4Se_3S_3$	5.26	5.65	2.32–2.37	2.18–2.24	−0.36	4.23	1.61
$Ni_4Se_3Te_3$	5.39	6.24	2.30–2.37	2.49–2.55	−0.18	3.92	0.77
$Ni_4S_3Te_3$	5.30	6.07	2.18–2.25	2.52–2.56	−0.27	4.06	0.49
$Co_4Se_3S_3$	5.52	5.65	2.34–2.40	2.18–2.27	−0.45	4.30	—
$Co_4Se_3Te_3$	5.40	6.08	2.30–2.37	2.51–2.54	−0.25	4.15	—
$Co_4S_3Te_3$	5.41	5.90	2.16–2.23	2.54–2.55	−0.35	4.12	—

lengths are not drastically different than those in the cases of $Pd_4Se_3S_3$ and $Pd_4Se_3Te_3$. In the meantime, the Pd–S bond length varies between 2.33–2.43 Å and the Pd–Te bond length varies between 2.61–2.67 Å in the two dimensional Janus materials. In the Ni derivatives, the lattice constant varies by a maximum of 0.42 Å and also the Ni–Se bond length varies between 2.30–2.37 Å, the Ni–S bond length varies between 2.18–2.25 Å and the Ni–Te bond length varies between 2.49–2.59 Å in the two dimensional Janus materials. In the Co derivatives, the lattice constant varies by a maximum of 0.22 Å and also the Co–Se bond length varies between 2.30–2.40 Å, the Co–S bond length varies between 2.16–2.27 Å and the Co–Te bond length varies between 2.51–2.55 Å in the two dimensional Janus materials in Table 2.

As expected, changing the chalcogen type of one face leads to differences in the thickness of the studied materials. It is seen that there is a total of 0.65 Å variation in thickness from the Pd_2Se_3 type, with the thicknesses of the Pd derivatives ranging between 3.21–4.07 Å. Also, there is a total of 0.17 Å variation in thickness from the Ni_2Se_3 type, with the thicknesses of the Ni derivatives ranging between 3.59–3.92 Å. Furthermore, it is seen that there is a total of 0.21 Å variation in thickness from the Co_2Se_3 type, with the thicknesses of the Co derivatives ranging between 3.53–3.94 Å. According to the Bader charge analysis, the transition metal type atoms donate most of the e in the $M_4Se_3S_3$ Janus structures; 0.20e is donated when M is Pd, 0.36e is donated when M is Ni and 0.45e is donated when M is Co.

The cohesive energies (per atom) of the Janus $M_4X_3Y_3$ (M = Pd, Ni and Co; X,Y = S, Se and Te) monolayers were calculated using the following relation:

$$E_{Coh} = [E(M_4X_3Y_3) - 4 \times E(M) - 3 \times E(X) - 3 \times E(Y)]/10 \quad (2)$$

where $E(M_2X_3)Y_3$ is the total energies of the $M_4X_3Y_3$ (M = Pd, Ni and Co; X, Y = S, Se and Te) monolayers, $E(M)$ is the single isolated atom energies of Ni, Pd and Co and $E(X)$ and $E(Y)$ are the single isolated atom energies of S, Se and Te. The calculated cohesive energies E_{Coh} for the $M_4X_3Y_3$ (M = Pd, Ni and Co; X, Y = S, Se and Te) monolayers are given in Table 2. Our results indicate that they are energetically stable and these materials can be synthesized.

21142 | *Phys. Chem. Chem. Phys.*, 2021, **23**, 21139–21147

This journal is © the Owner Societies 2021
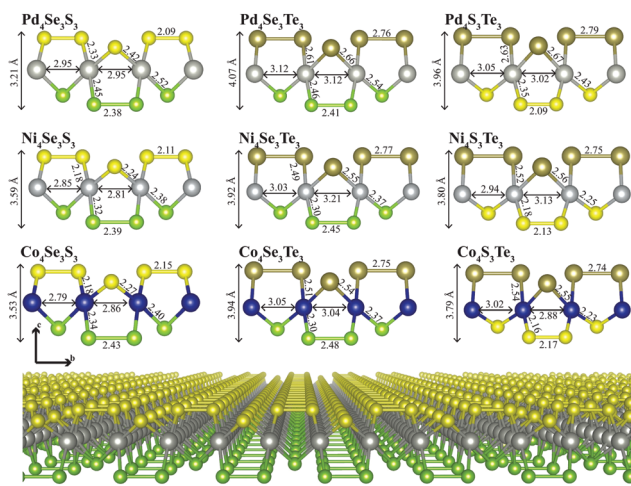
The band structures of the Pd- and Ni-based Janus $M_4X_3Y_3$ (M = Pd, Ni, and X, Y = S, Se, Te) monolayers were calculated using HSE + SOC and the band structures of the Co-based Janus $M_4X_3Y_3$ (M = Co and X, Y = S, Se, Te) monolayers with GGA+U were calculated, which are presented in Fig. 4. $Pd_4Se_3S_3$, $Pd_4Se_3Te_3$ and $Pd_4S_3Te_3$ are indirect band gap semiconductors with energy band gaps of 1.22 (VBM: Γ – CBM: S), 1.05 (VBM: X – CBM: Y) and 0.61(VBM: X – CBM: Y) eV, respectively. $Ni_4Se_3S_3$, $Ni_4Se_3Te_3$ and $Ni_4S_3Te_3$ are indirect band gap semiconductors with energy band gaps of 1.61 (VBM: X – CBM: Γ), 0.77 (VBM: S – CBM: Y) and 0.49 (VBM: S – CBM: Y) eV, respectively (see Table 1). As discussed above, this is due to Co^{2+} ($3d^7$) having unpaired electrons, which give rise to the magnetic state of the Co_2Se_3 monolayer. While pristine Co_2Se_3 is calculated to show half-metallicity (HM) with a moderate band gap (1.01 eV) with large intrinsic ferromagnetism, the HM behaviour of the Janus $Co_4Se_3Te_3$ and $Co_4S_3Te_3$ monolayers disappears and $Co_4Se_3S_3$ remains a HM with a moderate band gap (0.85 eV) (see Fig. 4).

3.4 Vibrational properties with Raman spectra and thermal properties

It is seen in Fig. 5 that the Pd variations and Ni variations have mostly positive phonon modes. $Co_4Se_3S_3$ and $Co_4S_3Te_3$ are quite stable at positive frequencies. It appears that $Pd_4Se_3Te_3$
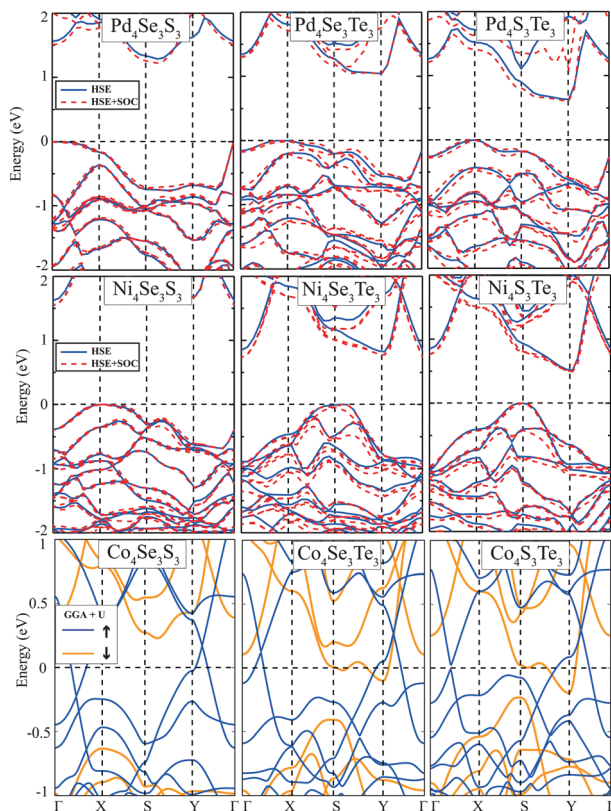
Fig. 4 Electronic band dispersions of HSE and HSE + SOC for $Pd_4Se_3S_3$, $Pd_4Se_3Te_3$, $Pd_4S_3Te_3$, $Ni_4Se_3S_3$, $Ni_4Se_3Te_3$, and $Ni_4S_3Te_3$ (HSE calculations are colored in blue and HSE + SOC calculations are indicated by dashed red lines) and GGA+U for $Co_4Se_3S_3$, $Co_4Se_3Te_3$, $Co_4S_3Te_3$ (the majority spin is colored in blue and the minority spin is in orange). The Fermi level is set to zero.

has phonon softening at the phonon branch with the highest frequency, which is calculated to be 241.3 cm^{-1}. On the other hand, the other Pd variations, $Pd_4Se_3S_3$ and $Pd_4S_3Te_3$, have phonon hardening at the phonon branch with the highest frequency. There is a 4.7 cm^{-1} difference between the highest frequency of $Pd_4Se_3S_3$ (429.5 cm^{-1}) and that of $Pd_4S_3Te_3$ (424.8 cm^{-1}) and about a 176.8 cm^{-1} difference from that of Pd_2Se_3 (252.7 cm^{-1}) at the Γ point. In the phonon spectrum of $Pd_4Se_3S_3$, there appears to be 1 triply degenerate and 4 doubly degenerate modes, while the other Pd variations show only singly and doubly degenerate modes, where $Pd_4Se_3Te_3$ acquires 1 doubly degenerate mode and $Pd_4S_3Te_3$ has 2 doubly degenerate modes.

The out-of-plane phonon mode of $Pd_4Se_3S_3$ at 143.6 cm^{-1} arises from the vibration of the Se and Pd atoms. There are two Raman active out-of-plane phonon modes at 228.4 and 283.6 cm^{-1} of $Pd_4Se_3S_3$, which can be seen in Fig. 6. It is also seen that the Raman active phonon mode at 257.9 cm^{-1} appears from the in-plane vibration of the Se atoms. The phonon mode with the highest frequency of the $Pd_4Se_3S_3$ dominates the remaining Raman active modes by the in-plane movement of the S atoms. $Pd_4Se_3Te_3$ has a Raman active phonon mode in the low-frequency regime at 99.5 cm^{-1} that appears from the out-of-plane motion of the Pd and Te atoms. The two Raman active modes at 153.7 and 110.1 cm^{-1} happen from the out-of-plane motion. The phonon mode at 177.3 cm^{-1} resembles the significant Raman active mode which occurs from the in-plane motion of the Te atoms and the out-of-plane motion of the Se atoms. An out-of-plane phonon mode occurs at 208.3 cm^{-1} and the phonon mode with the highest frequency results from the in-plane motion of the Se atoms. The Janus structure $Pd_4Se_3Te_3$ has phonon softening and the other types have phonon hardening at the phonon mode with the highest frequency and the Ni derivatives are similar; $Ni_4Se_3Te_3$ has phonon softening at the phonon branch with the highest frequency, which is calculated to be 294.6 cm^{-1}. On the other hand, the other Ni variations, $Ni_4Se_3S_3$ and $Ni_4S_3Te_3$, have phonon hardening at the phonon branch with the highest frequency. There is a 37.9 cm^{-1} difference between the highest frequency of $Ni_4Se_3S_3$ (411.6 cm^{-1}) and that of $Ni_4S_3Te_3$ (376.7 cm^{-1}) and about a 96.5 cm^{-1} difference from that of Ni_2Se_3 (315.1 cm^{-1}) at the Γ point. In the Ni variations, it is seen that $Ni_4S_3Te_3$ has a triply degenerate mode. The doubly degenerate mode number of the Ni Janus structures are 3, 4 and 6 for $Ni_4Se_3S_3$, $Ni_4Se_3Te_3$ and $Ni_4S_3Te_3$, respectively.

The Ni Janus structures seem to be more Raman active than the Pd variations. Firstly, the Raman active phonon modes of $Ni_4Se_3S_3$ can be seen in Fig. 6. The phonon mode at 146.7 cm^{-1} occurs from the in-plane motion of the Ni atoms and the out-of-plane motion of the Se atoms. A quite smaller Raman active phonon mode can be seen at 146.7 cm^{-1}; on the other hand, the dominant Raman active phonon mode of $Ni_4Se_3S_3$ vibrates at the doubly degenerate mode at 244.9 cm^{-1}. A singly degenerate mode at 332.8 cm^{-1} occurs from the in-plane motion of the Ni and the out-of-plane motion of the Se and S atoms that have quite prominent Raman activity. The phonon mode with

This journal is © the Owner Societies 2021

Phys. Chem. Chem. Phys., 2021, **23**, 21139–21147 | **21143**
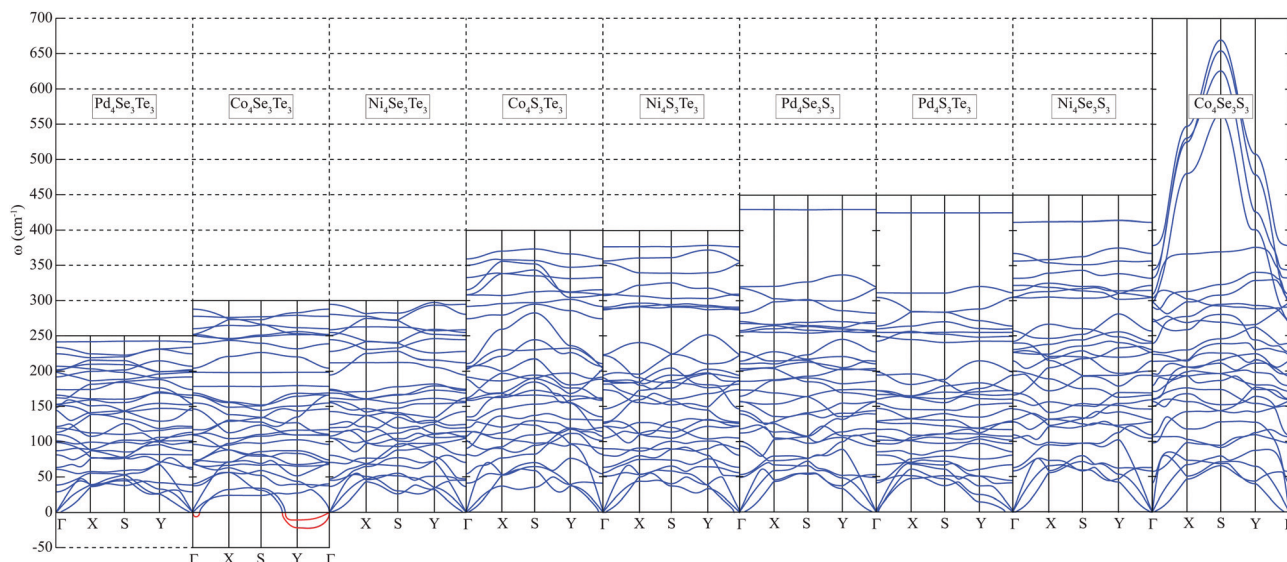
Fig. 5   Vibrational band dispersions of $Pd_4Se_3S_3$, $Pd_4Se_3Te_3$, $Pd_4S_3Te_3$, $Co_4Se_3S_3$, $Co_4Se_3Te_3$, $Co_4S_3Te_3$, $Ni_4Se_3S_3$, $Ni_4Se_3Te_3$ and $Ni_4S_3Te_3$.
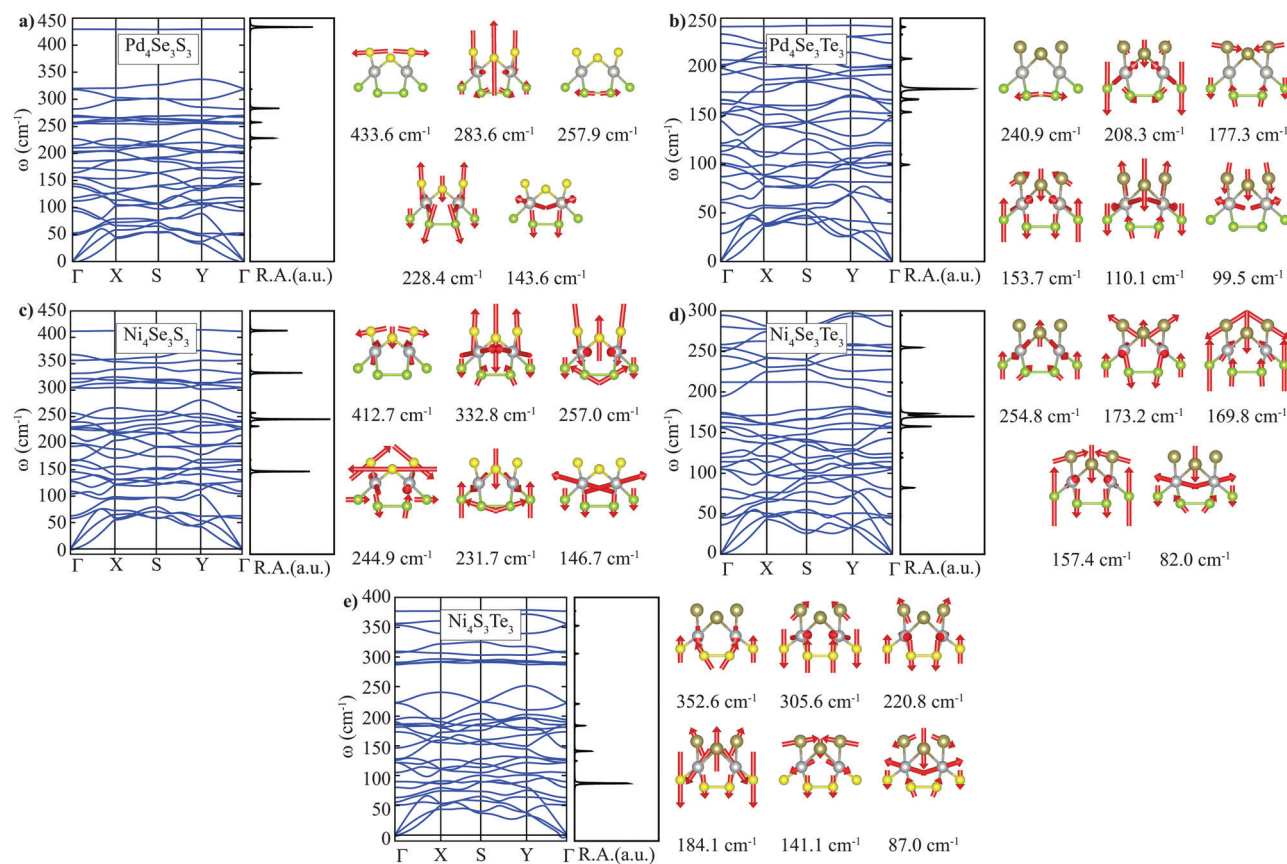
Fig. 6   Raman spectra with phonon bands of $Pd_4Se_3S_3$, $Pd_4Se_3Te_3$, $Ni_4Se_3S_3$, $Ni_4Se_3Te_3$ and $Ni_4S_3Te_3$.

the highest frequency occurs from the vibration of S and Ni atoms.

The Raman activity of the two-dimensional Janus material $Ni_4Se_3S_3$ is studied. A Raman active phonon mode arises at the low-frequency regime (82.0 cm^{-1}), occurring from the out-of-plane vibrations of the Se and Te atoms and the in-plane motion of the Ni atoms. A doubly degenerate mode at 157.4 cm^{-1} has prominent Raman activity. The most dominant
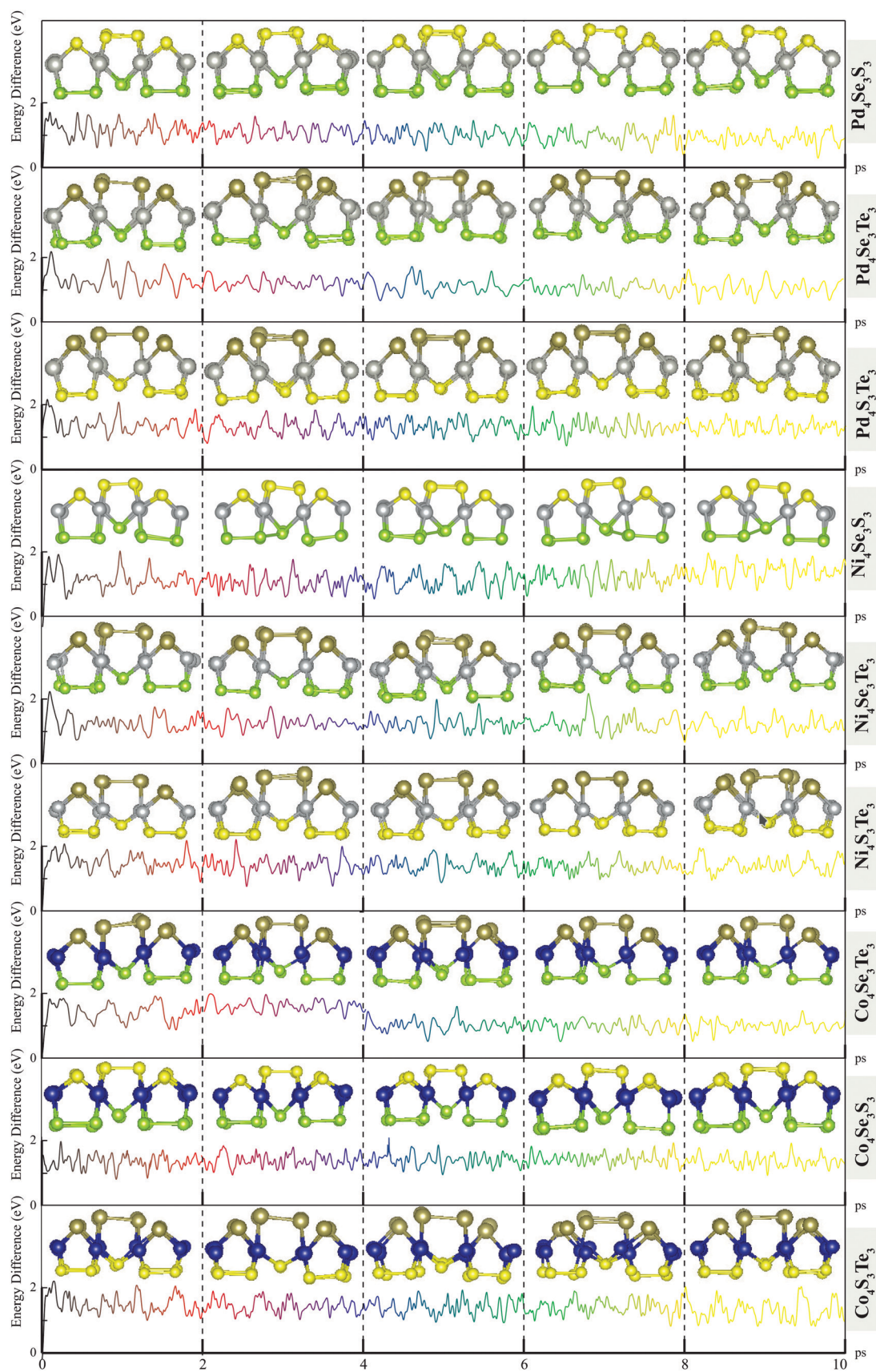
Fig. 7 The fluctuations of the total energies of the Janus $M_4X_3Y_3$, where M = Pd, Co and Ni and X = Se, S and Te, during the AIMD simulations at 300 K. The insets are snapshots of the structures at the end of the simulations at the end of each 2 ps.

This journal is © the Owner Societies 2021

Phys. Chem. Chem. Phys., 2021, **23**, 21139–21147 | **21145**

Raman active out-of-plane phonon mode occurs at 169.8 cm^{-1}. On the other hand, a single degenerate mode with minor Raman activity with the out-of-plane motion of the Se and Te atoms and the in-plane motion of the Ni atoms is seen to vibrate at 173.2 cm^{-1}. It is also seen that an average Raman active phonon mode with out-of-plane motion oscillates at 254.8 cm^{-1}.

In terms of the Raman activity, $Ni_4S_3Te_4$ differs from the other materials whose Raman activities were studied. The most dominant Raman mode occurs in the low-frequency regime at 87.0 cm^{-1}. A single degenerate Raman active phonon mode with the out-of-plane motion of the S and Ni atoms and the in-plane motion of the Te atoms is found at 141.1 cm^{-1}. A breathing-like Raman active mode at 184.1 cm^{-1} results from the out-of-plane motion of the atoms. The two phonon modes with nearly similar atomic motions at 220.8 and 305.6 cm^{-1} develop from the out-of-plane oscillations of the S and Te atoms and the in-plane vibrations of Ni atoms, respectively. The phonon mode at 352.6 cm^{-1} results from most of the vibration of the out-of-plane motions of the S atoms.

For the Co variations, the Janus structures $Co_4Se_3S_3$ and $Co_4S_3Te_3$ appear to have higher frequencies than that of Co_2Se_3 (378.0 and 359.3 cm^{-1}, respectively) at the Γ point. Another important thing to note is that while the peak at the S point of Co_2Se_3 was at 491.4 cm^{-1}, $Co_4Se_3S_3$ has a significantly higher frequency at 669.5 cm^{-1}. On the other hand, $Co_4Se_3S_3$ shows 2 triply degenerate modes and 4 doubly degenerate modes, while $Co_4S_3Te_3$ has 3 doubly degenerate modes.

In addition, the thermal stabilities are examined by performing *ab initio* molecular dynamics (AIMD) simulations using the *NVT* ensemble with a fixed particle number, volume and temperature. For the AIMD simulations, a 40-atom supercell is used for each single layer with a k-mesh of $4 \times 4 \times 1$. The thermal stability investigations start with the optimized structure of the Janus $M_4X_3Y_3$ single layers, where M = Pd, Co and Ni and X = Se, S and Te, at 0 K. We further extend the thermal stability calculations up to room temperature (300 K). During the simulations, the temperature is kept at the given temperatures and the fluctuations of the total energy and the changes of these Janus atomic structures during the simulations are shown in Fig. 7. The time step is set to 1 fs (1000 steps) with a total simulation time of 10 ps. The structure snapshots are taken at the end of the each simulation every 2 ps. The fluctuations of the total energy are shown on top of each other for each 2 ps. As can be seen in Fig. 7, none of the single layers undergo structural reconstruction at 300 K, indicating the thermal stability. The energies of these systems systematically correspond with their optimized geometries, confirming their thermal stability of Janus $M_4X_3Y_3$ single layers, where M = Pd, Co and Ni and X = Se, S and Te, even at 300 K.

4 Conclusion

In summary, we have investigated the structural, electronic and mechanical properties of Janus single layers of $M_4X_3Y_3$, where

M = Pd, Co and Ni and X = Se, S and Te. Phonon spectrum analysis and high temperature *ab initio* MD calculations reveal the dynamical stability of these monolayers, apart from $Co_4Se_3Te_3$. Due to the contribution of the d orbitals, the dynamical stability of $Co_4Se_3Te_3$ should be investigated with some corrections in the future. The vibrational properties were computed with the aim of understanding and characterizing the origin of the Raman active peaks. By making Janus structures of these transition metal chalcogenides to investigate the mechanical properties of Janus single layers of $M_4X_3Y_3$, the electronic band dispersions were shown to vary with using heavier/lighter chalcogen atoms. To get more accurate electronic band structures of the pristine and Janus $M_4X_3Y_3$ monolayers, where M = Pd, Co and Ni and X = Se, S and Te, the HSE + SOC approximation is taken into account for the Pd-based pristine and Janus $Pd_4X_3Y_3$ monolayers, where X = Se, S and Te, and the Ni-based pristine and Janus $Ni_4X_3Y_3$ monolayers, where X = Se, S and Te, while GGA+U is taken into account for the Co-based pristine and Janus $Co_4X_3Y_3$ monolayers, where X = Se, S and Te. Our results showed that $Pd_4Se_3S_3$, $Pd_4Se_3Te_3$ and $Pd_4S_3Te_3$ are indirect band gap semiconductors with energy band gaps of 1.22 (VBM: Γ – CBM: S), 1.05 (VBM: X – CBM: Y) and 0.61(VBM: X – CBM: Y) eV, respectively. $Ni_4Se_3S_3$, $Ni_4Se_3Te_3$ and $Ni_4S_3Te_3$ are indirect band gap semiconductors with energy band gap of 1.61 (VBM: X – CBM: Γ), 0.77 (VBM: S – CBM: Y) and 0.49 (VBM: S – CBM: Y) eV, respectively. Co^{2+} (3d^7) has unpaired electrons, which give rise to the magnetic state of the Co_2Se_3 monolayer. While pristine Co_2Se_3 was calculated to show half-metallicity (HM) with a moderate band gap (1.01 eV) and large intrinsic ferromagnetism, the HM behaviour of the Janus $Co_4Se_3Te_3$ and $Co_4S_3Te_3$ monolayers disappears and $Co_4Se_3S_3$ remained a HM with a moderate band gap (0.85 eV). In addition, the *ab initio* MD calculations confirmed the stability of the Janus structures at room temperature. Our work will be useful in the understanding and design for possible potential applications based on Janus 2D materials.

Conflicts of interest

There are no conflicts to declare.

Acknowledgements

Notes and references

1 K. S. Novoselov, A. K. Geim, S. V. Morozov, D. Jiang, Y. Zhang, S. V. Dubonos, I. V. Grigorieva and A. A. Firsov, *Science*, 2004, **306**, 666–669.

21146 | *Phys. Chem. Chem. Phys.*, 2021, **23**, 21139–21147

This journal is © the Owner Societies 2021

2 S. Cahangirov, M. Topsakal, E. Aktürk, H. Sahin and S. Ciraci, *Phys. Rev. Lett.*, 2009, **102**, 236804.

3 B. Akgenc, *J. Mater. Sci.*, 2019, **54**, 9543–9552.

4 M. Baskurt, I. Eren, M. Yagmurcukardes and H. Sahin, *Appl. Surf. Sci.*, 2020, **508**, 144937.

5 C. Zhi, Y. Bando, C. Tang, H. Kuwahara and D. Golberg, *Adv. Mater.*, 2009, **21**, 2889–2893.

6 J. H. Warner, M. H. Rummeli, A. Bachmatiuk and B. Buchner, *ACS Nano*, 2010, **4**, 1299–1304.

7 C. Ekuma, V. Dobrosavljević and D. Gunlycke, *Phys. Rev. Lett.*, 2017, **118**, 106404.

8 Z. Ling, C. E. Ren, M.-Q. Zhao, J. Yang, J. M. Giammarco, J. Qiu, M. W. Barsoum and Y. Gogotsi, *Proc. Natl. Acad. Sci. U. S. A.*, 2014, **111**, 16676–16681.

9 M. Naguib, J. Come, B. Dyatkin, V. Presser, P.-L. Taberna, P. Simon, M. W. Barsoum and Y. Gogotsi, *Electrochem. Commun.*, 2012, **16**, 61–64.

10 X. Liang, A. Garsuch and L. F. Nazar, *Angew. Chem.*, 2015, **127**, 3979–3983.

11 A. Bafekry, M. Yagmurcukardes, B. Akgenc, M. Ghergherehchi and C. V. Nguyen, *J. Phys. D: Appl. Phys.*, 2020, **53**, 355106.

12 A. Bafekry, B. Akgenc, M. Ghergherehchi and F. Peeters, *J. Phys.: Condens. Matter*, 2020, **32**, 355504.

13 B. Akgenc, *Solid State Commun.*, 2019, **303–304**, 113739.

14 B. Akgenc, A. Mogulkoc and E. Durgun, *J. Appl. Phys.*, 2020, **127**, 084302.

15 S. Manzeli, D. Ovchinnikov, D. Pasquier, O. V. Yazyev and A. Kis, *Nat. Rev. Mater.*, 2017, **2**, 17033.

16 Q. H. Wang, K. Kalantar-Zadeh, A. Kis, J. N. Coleman and M. S. Strano, *Nat. Nanotechnol.*, 2012, **7**, 699–712.

17 S. Demirci, N. Avazl, E. Durgun and S. Cahangirov, *Phys. Rev. B*, 2017, **95**, 115409.

18 D. Jariwala, V. K. Sangwan, L. J. Lauhon, T. J. Marks and M. C. Hersam, *ACS Nano*, 2014, **8**, 1102–1120.

19 X. Hong, J. Kim, S.-F. Shi, Y. Zhang, C. Jin, Y. Sun, S. Tongay, J. Wu, Y. Zhang and F. Wang, *Nat. Nanotechnol.*, 2014, **9**, 682.

20 S. Tongay, J. Zhou, C. Ataca, K. Lo, T. S. Matthews, J. Li, J. C. Grossman and J. Wu, *Nano Lett.*, 2012, **12**, 5576–5580.

21 A. V. Kuklin and H. Ågren, *Phys. Rev. B*, 2019, **99**, 245114.

22 A. D. Oyedele, S. Yang, L. Liang, A. A. Puretzky, K. Wang, J. Zhang, P. Yu, P. R. Pudasaini, A. W. Ghosh and Z. Liu, *et al.*, *J. Am. Chem. Soc.*, 2017, **139**, 14090–14097.

23 L. Pi, C. Hu, W. Shen, L. Li, P. Luo, X. Hu, P. Chen, D. Li, Z. Li and X. Zhou, *et al.*, *Adv. Funct. Mater.*, 2020, **2006774**, 2006774–2006783.

24 M. Yagmurcukardes and F. Peeters, *Phys. Rev. B*, 2020, **101**, 155205.

25 X. Zhao, Z. Yang, J. Guo, G. Hu, W. Yue, X. Yuan and J. Ren, *Sci. Rep.*, 2020, **10**, 1–8.

26 S. Deng, L. Li and Y. Zhang, *ACS Appl. Nano Mater.*, 2018, **1**, 1932–1939.

27 S. Ahmad and G. Schreckenbach, *Mater. Today Commun.*, 2020, **24**, 100976.

28 D. Qin, P. Yan, G. Ding, X. Ge, H. Song and G. Gao, *Sci. Rep.*, 2018, **8**, 1–8.

29 Y.-S. Lan, X.-R. Chen, C.-E. Hu, Y. Cheng and Q.-F. Chen, *J. Mater. Chem. A*, 2019, **7**, 11134–11142.

30 F. Ersan and C. Ataca, *Phys. Rev. Appl.*, 2020, **13**, 064008.

31 G. Chaney, A. Ibrahim, F. Ersan, D. Çakır and C. Ataca, *ACS Appl. Mater. Interfaces*, 2021, **13**(30), 36388–36406.

32 Y. Z. Abdullahi, Z. D. Vatansever, F. Ersan, U. Akinci, O. U. Akturk and E. Akturk, *Phys. Chem. Chem. Phys.*, 2021, **23**, 6107–6115.

33 J. Lin, S. Zuluaga, P. Yu, Z. Liu, S. T. Pantelides and K. Suenaga, *Phys. Rev. Lett.*, 2017, **119**, 016101.

34 X. Zhu, F. Li, Y. Wang, M. Qiao and Y. Li, *J. Mater. Chem. C*, 2018, **6**, 4494–4500.

35 X. Xu, J. Robertson and H. Li, *Phys. Chem. Chem. Phys.*, 2020, **22**, 7365–7373.

36 S. S. Naghavi, J. He, Y. Xia and C. Wolverton, *Chem. Mater.*, 2018, **30**, 5639–5647.

37 X. Li, S. Zhang, Y. Guo, F. Q. Wang and Q. Wang, *Nanomaterials*, 2018, **8**, 832.

38 J. Chen, G. H. Ryu, S. Sinha and J. H. Warner, *ACS Nano*, 2019, **13**, 8256–8264.

39 P. Lv, G. Tang, C. Yang, J. Deng, Y. Liu, X. Wang, X. Wang and J. Hong, *2D Mater.*, 2018, **5**, 045026.

40 W. Xiong, K. Huang and S. Yuan, *J. Mater. Chem. C*, 2019, **7**, 13518–13525.

41 A.-Y. Lu, H. Zhu, J. Xiao, C.-P. Chuu, Y. Han, M.-H. Chiu, C.-C. Cheng, C.-W. Yang, K.-H. Wei and Y. Yang, *et al.*, *Nat. Nanotechnol.*, 2017, **12**, 744–749.

42 J. Zhang, S. Jia, I. Kholmanov, L. Dong, D. Er, W. Chen, H. Guo, Z. Jin, V. B. Shenoy and L. Shi, *et al.*, *ACS Nano*, 2017, **11**, 8192–8198.

43 A. B. Maghirang, Z.-Q. Huang, R. A. B. Villaos, C.-H. Hsu, L.-Y. Feng, E. Florido, H. Lin, A. Bansil and F.-C. Chuang, *npj 2D Mater. Appl.*, 2019, **3**, 1–8.

44 L. Zhang, Z. Yang, T. Gong, R. Pan, H. Wang, Z. Guo, H. Zhang and X. Fu, *J. Mater. Chem. A*, 2020, **8**, 8813–8830.

45 R. Li, Y. Cheng and W. Huang, *Small*, 2018, **14**, 1802091.

46 P. E. Blöchl, *Phys. Rev. B: Condens. Matter Mater. Phys.*, 1994, **50**, 17953.

47 J. P. Perdew, K. Burke and M. Ernzerhof, *Phys. Rev. Lett.*, 1996, **77**, 3865.

48 G. Kresse and J. Hafner, *Phys. Rev. B: Condens. Matter Mater. Phys.*, 1993, **47**, 558.

49 G. Kresse and J. Furthmüller, *Phys. Rev. B: Condens. Matter Mater. Phys.*, 1996, **54**, 11169.

50 S. Grimme, S. Ehrlich and L. Goerigk, *J. Comput. Chem.*, 2011, **32**, 1456–1465.

51 J. Heyd, G. E. Scuseria and M. Ernzerhof, *J. Chem. Phys.*, 2003, **118**, 8207–8215.

52 S. Dudarev, G. Botton, S. Savrasov, C. Humphreys and A. Sutton, *Phys. Rev. B: Condens. Matter Mater. Phys.*, 1998, **57**, 1505.

53 G. Henkelman, A. Arnaldsson and H. Jónsson, *Comput. Mater. Sci.*, 2006, **36**, 354–360.

54 X. Gonze and C. Lee, *Phys. Rev. B: Condens. Matter Mater. Phys.*, 1997, **55**, 10355.

55 F. Oba, A. Togo, I. Tanaka, J. Paier and G. Kresse, *Phys. Rev. B: Condens. Matter Mater. Phys.*, 2008, **77**, 245202.

56 D. Alfè, *Comput. Phys. Commun.*, 2009, **180**, 2622–2633.

This journal is © the Owner Societies 2021

Phys. Chem. Chem. Phys., 2021, **23**, 21139–21147 | **21147**